Extended X-ray Absorption Fine Structure Studies of the Anion Complexes of FeZn Uteroferrin†

Xuedong Wang and Lawrence Que, Jr.*

Department of Chemistry & Center for Metals in Biocatalysis, University of Minnesota, Minneapolis, Minnesota 55455

Received January 21, 1998; Revised Manuscript Received March 26, 1998

ABSTRACT: Molybdate and tungstate are strong inhibitors of the purple acid phosphatases. The binding modes of these anions to the FeZn derivative of uteroferrin, the purple acid phosphatase from porcine uterus (FeZnUf), have been characterized by X-ray absorption spectroscopy at both the iron and zinc K-edges. Pre-edge data show that both FeZnUf·MoO_4 and FeZnUf·WO_4 have six-coordinate iron sites. Analysis of the EXAFS regions shows that the iron sites of both molybdate and tungstate complexes are best simulated by a shell of three O or N atoms at 2.08−2.09 Å and a shell of two O or N atoms at 1.93−1.95 Å. On the other hand, the zinc sites have shells of five O or N atoms at ∼ 2.1 Å and one O or N atom at ∼ 2.5 Å. Because of the higher resolution of the FeZnUf·MoO_4 data, the main shell at ∼2.1 Å can be further split into shells of four O or N at 2.04 Å and one O or N at 2.22 Å, the latter being associated with a molybdate oxygen. Outer-sphere EXAFS analysis indicates an Fe−Zn separation of ∼3.4 Å for both FeZnUf·MoO_4 and FeZnUf·WO_4, Fe−Mo/W distances of 3.2 Å, and Zn−Mo/W distances of 3.6−3.7 Å. Thus, molybdate and tungstate bridge the FeZn active site like phosphate, but do so unsymmetrically. The asymmetric bidentate bridging mode of molybdate and tungstate helps explain the effect of these anions on the redox properties of the diiron uteroferrin.

Purple acid phosphatases (PAPs)[1] belong to a class of metallohydrolases containing bimetallic active sites (*1*) that catalyze the hydrolysis of phosphate esters in vitro and contain a (μ-hydroxo)(μ,η^1-aspartato)dimetal active site (Figure 1) (*2*,*3*) similar to those found for protein phosphatase 1 (PP-1) (*4*, *5*) and protein phosphatase 2B (calcineurin) (*6*, *7*). Furthermore, there is strong amino acid sequence homology between PAPs and PPs in their catalytic regions (*8*). These observations have led to a hypothesis that PAPs and PPs may have similar functions in vivo. It is well-known that PPs play key roles in signal transduction in eukaryotic organisms (*9*). PP-1 is the major phosphatase that regulates glycogen metabolism in response to insulin and adrenalin (*10*). PP2B or calcineurin is essential in T-cell activation and a common target of two immunosuppressive drugs, cyclosporin A and FK506 (*11*).

The crystal structure of kidney bean PAP (KBPAP) at pH 5 shows an active site with an Fe(III)Zn(II) center bridged by a monodentate aspartate and presumably a hydroxide (Figure 1), resulting in an Fe−Zn separation of 3.26 Å (*2*, *3*). The Fe(III) site is terminally coordinated by a tyrosine, histidine, and monodentate aspartate, while the Zn(II) site is terminally coordinated by two histidines and an asparagine. The Fe(III)Fe(II) active sites of Uf and other mammalian PAPs are believed to be similar to that of KBPAP, because all metal ligands are conserved between KBPAP and the mammalian PAPs (*12*). In addition, the Fe(II) site in the mammalian PAPs can be replaced by Zn(II) without loss of activity (*13*, *14*), while KBPAP can be converted to an active

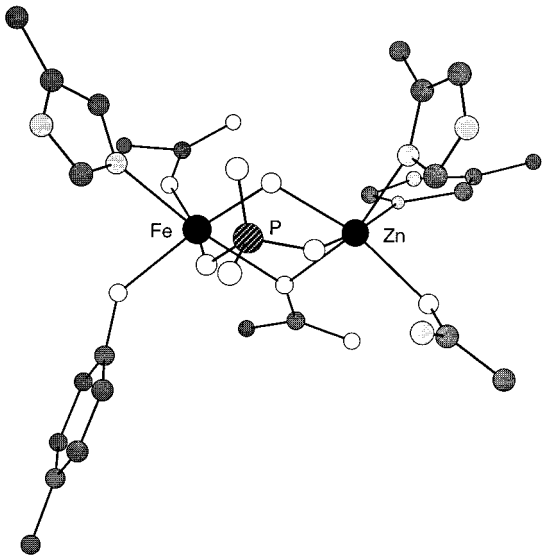

FIGURE 1: KBPAP active site (adapted from ref *3*).

† This work was supported by a grant from the National Science Foundation (MCB-9405723, L.Q.). Beamline X9 at the NSLS at BNL is supported by the National Institutes of Health (RR-001633).

* To whom correspondence should be addressed. Fax: (612) 624-7029. E-mail: que@chem.umn.edu.

[1] Abbreviations: EPR, electron paramagnetic resonance; ESEEM, electron spin-echo envelope modulation; EXAFS, extended X-ray absorption fine structure; FeZnUf, FeZn derivative of uteroferrin; FeZnUf·PO_4, phosphate complex of FeZnUf; FeZnUf·MoO_4, molybdate complex of FeZnUf; FeZnUf·WO_4, tungstate complex of FeZnUf; ImH, imidazole; KBPAP, kidney bean purple acid phosphatase; OBz, benzoate; PAP, purple acid phosphatase; PP, Ser/Thr protein phosphatase; PP-1, protein phosphatase 1; Uf, uteroferrin; Uf_r, reduced uteroferrin; XANES, X-ray absorption near-edge structure; XAS, X-ray absorption spectroscopy; XDK, *m*-xylenediamine bis(Kemp's triacid)-imide.

S0006-2960(98)00150-0 CCC: $15.00
Published on Web 05/07/1998

Fe(III)Fe(II) form with spectroscopic properties very similar to those of the mammalian PAPs (*15*, *16*).

Phosphate, the product, and other tetraoxo anions are inhibitors of both Uf and FeZnUf (*17*). Phosphate and arsenate are weak competitive inhibitors with millimolar K_i values. Phosphate has been found to act as a bidentate bridge between the two metal centers according to an EXAFS analysis of FeZnUf·PO_4 (*18*) and a crystallographic study of KBPAP·PO_4 (*3*). In contrast, molybdate and tungstate are potent competitive inhibitors with K_i values in the micromolar range (*17*). Molybdate also affects the properties of the dinuclear centers of Uf and FeZnUf in a manner very different from that of phosphate and arsenate. While phosphate and arsenate engender EPR spectra of rhombic symmetry, molybdate gives rise to axial EPR signals (*19*). More interestingly, phosphate and arsenate shift the redox potential of Uf to a more negative value, while molybdate shifts the potential to a more positive value (*20*), in line with the different susceptibilities of Uf to aerobic oxidation in the presence of these anions (*17*). Recent CD and MCD studies on uteroferrin−anion complexes also show that molybdate affects the dinuclear active site in a manner different from that of phosphate (*21*). On the basis of these biochemical, spectroscopic, and electrochemical results, molybdate and tungstate very likely interact with the dinuclear center in a mode different from that of phosphate and arsenate. This notion is contradicted by the crystal structure of the KBPAP−tungstate complex which shows an active site nearly identical to that of the KBPAP−phosphate complex (*3*). Here we report the use of X-ray absorption spectroscopy in studying the dinuclear centers of FeZnUf·MoO_4 and FeZnUf·WO_4 and elucidate the mode of molybdate and tungstate binding. These data allow a comparison among the molybdate, tungstate, and phosphate complexes of FeZnUf and provide insight into how they interact differently with the dinuclear center of the enzyme.

EXPERIMENTAL PROCEDURES

Steady-State Kinetic Studies. Uteroferrin was isolated and purified according to literature procedures (*22*, *23*). FeZnUf was then reconstituted (*24*), and metal analysis gave values of 1.0 ± 0.1 Fe and 1.0 ± 0.1 Zn atoms per molecule. FeZnUf was fully active as native uteroferrin with a specific activity of about 350 units/mg (with *p*-nitrophenyl phosphate as the substrate and the release of *p*-nitrophenol being measured at 390 nm). K_i values were determined from steady-state Michaelis−Menten enzyme kinetics studies and extracted from fits to Lineweaver−Burke plots of the data. Buffers used for the pH dependence studies were as follows: 0.1 M acetate/0.2 M NaCl (pH 4−5.5), 0.1 M imidazole/0.2 M NaCl (pH 6−6.5), and 0.1 M Tris-HCl/0.2 M NaCl (pH 7−7.5).

X-ray Absorption Spectroscopy. Samples of FeZnUf·MoO_4 and FeZnUf·WO_4 were prepared by respectively adding 1.1 equiv of molybdate and tungstate to the concentrated FeZnUf solution in acetate buffer at pH 4.9. EPR spectra of the FeZnUf·MoO_4 and FeZnUf·WO_4 samples verified the absence of free FeZnUf as well as the absence of diiron Uf. The XAS samples were diluted with glycerol (20 vol %) to prevent ice crystal formation when the samples were frozen in gold-plated copper sample holders.

X-ray absorption data at both the iron and zinc K-edges of FeZnUf·MoO_4 and FeZnUf·WO_4 were collected at Beamline X9 of the National Synchrotron Light Source (NSLS) at Brookhaven National Laboratory. The X-ray absorption spectra at the iron K-edge were collected between 6.95 and 8.0 keV, and the monochromator was calibrated using the edge energy of iron foil at 7113.6 eV. The Zn-edge spectra were collected between 9.46 and 10.35 keV, and the monochromator was calibrated using the edge energy of zinc foil at 9662.0 eV. XAS data were obtained in the fluorescence mode from protein samples frozen at 77 K. The A_{exp} (C_f/C_o) was determined from an incident (C_o) ionization detector and a final fluorescence (C_f) detector, which was a 13-element Ge solid-state detector (Canberra).

The treatment of raw EXAFS data which yields χ is discussed in detail in review articles (*25*, *26*). A modification of the EXAPLT program was employed to extract χ from A_{exp} by using a cubic spline function, including preliminary baseline correction and correction of fluorescence data for thickness effects and detector response (*27*). The refinements reported were on $k^3\chi$ data, and the function minimized was $R = [\sum k^6(\chi_c - \chi)^2/N]^{1/2}$, where the sum is over N data points between 2 and 15 Å^{-1}.

Single-scattering EXAFS theory allows the total EXAFS spectrum to be described as the sum of shells of separately modeled atoms

$$\chi_c = \sum nA[f(k)k^{-1}r^{-2}\exp(-2\sigma^2k^2)\sin[2kr + \alpha(k)]]$$

where n is the number of atoms in the shell, $k = [8\pi^2m_e(E - E_0 + \Delta E)/h^2]^{1/2}$, and σ^2 is the Debye−Waller factor (*27*). The amplitude reduction factor (A) and the shell-specific edge shift (ΔE) are empirical parameters that partially compensate for imperfections in the theoretical amplitude and phase functions (*28*). Phase and amplitude functions were theoretically calculated using a curved-wave formalism (*29*). A variation of FABM (fine adjustment based on models) was used here in the analysis procedure with theoretical phase and amplitude functions (*30*). In each shell, two parameters were refined at one time (r and n or σ^2), while A and ΔE values were determined by using a series of crystallographically characterized model complexes. The fitting results indicate the average metal−ligand distances, the type and number of scatterers, and the Debye−Waller factors which can be used to evaluate the distribution of Fe− or Zn−ligand bond lengths in each shell. The EXAFS goodness of fit criterion applied here is

$$\epsilon^2 = [(N_{idp}/\nu)\sum(\chi_c - \chi)^2/\sigma^2]/N$$

as recommended by the International Committee on Standards and Criteria in EXAFS (*31*, *32*), where ν is the number of degrees of freedom calculated as $\nu = N_{idp} - N_{var}$, N_{idp} is the number of independent data points, and N_{var} is the number of variables that are refined. N_{idp} is calculated with the equation $N_{idp} = 2\Delta k\Delta R/\pi + 2$ (*33*). The use of ϵ^2 as the criterion for the goodness of fit allows us to compare fits using different numbers of variable parameters.

The pre-edge areas were calculated by subtracting an arctangent function from the data and normalizing with respect to the edge jump height. The background function was determined by a least-squares fit of an arctangent

Table 1: pH Dependence of K_i for Synthesis of Molybdate and Phosphate with FeZnUf

pH	K_i(molybdate) (μM)	K_i(phosphate) (mM)
4.0	1.8	2.0
4.5	2.1	2.2
4.9	2.4	3.6
5.5	15	4.6
6.0	18	5.2
6.5	120	11
7.0	630	27
7.5	1100	35

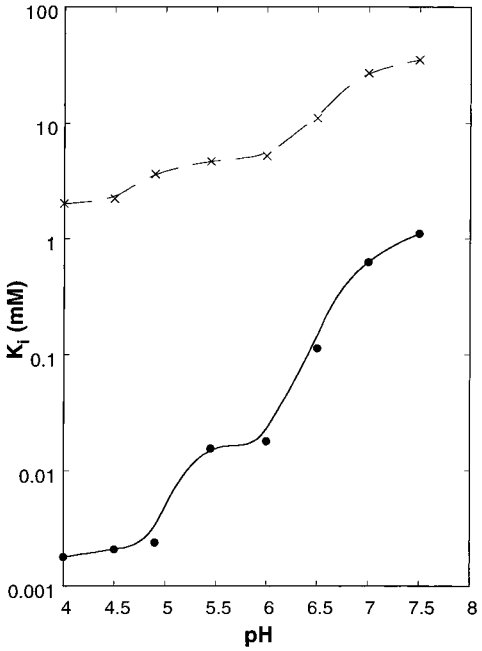

FIGURE 2: pH dependence of K_i values for phosphate (×) and molybdate (●) inhibition of FeZnUf.

together with a first-order polynomial to the data below the inflection point to the edge (*34*). The edge jump was determined by fitting a first-order polynomial to the data. The pre-edge area after the background subtraction was obtained by integrating over a range of about 8 eV. This range centered on the peak, and any residual background function was interpolated over that range. The difference between the two lines at the inflection point was used as the normalization factor for the pre-edge area.

RESULTS

pH Dependence of K_i. Phosphate and molybdate are both competitive inhibitors of Uf and FeZnUf (*17*). However, their affinities for the active site differ by 3 orders of magnitude. To gain further insight into these interactions, we have measured the K_i values of molybdate and phosphate at different pHs (Table 1 and Figure 2). We confirm that the inhibition behavior of both phosphate and molybdate are competitive at all pH values studied. The binding affinities of molybdate and phosphate for FeZnUf both decrease as the pH increases. Two apparent p*K* values, 5.5 and 7.0, can be derived from Figure 2 for both molybdate and phosphate. These two p*K*s most likely are associated with two conserved histidine residues in the active site that interact with the anions by hydrogen bonds as demonstrated in the crystal structures of KBPAP·PO_4 and KBPAP·WO_4 (*3*).

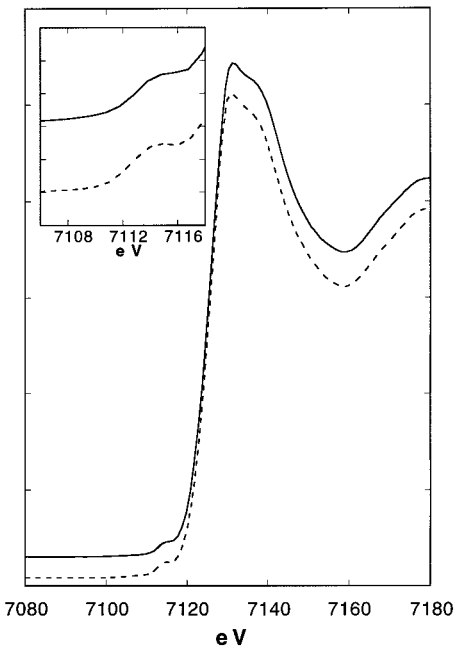

FIGURE 3: Fe K-edge XANES spectra of FeZnUf·MoO_4 (—) and FeZnUf·WO_4 (- - -). The inset is a magnification of the 1s → 3d pre-edge transition.

Pre-Edge Data. XANES studies and molecular orbital calculations on iron model compounds have demonstrated that the intensity of the 1s → 3d pre-edge feature relative to the edge jump can be correlated with the metal coordination geometry (*34*, *35*). In general, the pre-edge peak intensity increases as the metal coordination environment deviates from inversion symmetry, and therefore, $I_{\text{tetrahedral}} > I_{5-\text{coord}} > I_{\text{octahedral}}$. From the pre-edge database for Fe(III) complexes, tetrahedral complexes have pre-edge peak areas ranging from 23 to 25 units, five-coordinate complexes from 12 to 19 units, and six- or seven-coordinate complexes from 6 to 9 units (*34*).

The positions of the Fe K-edges of FeZnUf·MoO_4 and FeZnUf·WO_4 (7124.1 and 7124.3 eV, respectively) are consistent with the iron being in the +3 oxidation state. The 1s → 3d pre-edge areas for FeZnUf·MoO_4 and FeZnUf·WO_4 are 7.9 and 8.8 units, respectively, as shown in Figure 3. These values are consistent with those found for six-coordinate mononuclear iron(III) complexes. Thus, the Fe(III) sites of both FeZnUf·MoO_4 and FeZnUf·WO_4 are six-coordinate.

First-Sphere EXAFS Analysis. The raw $k^3\chi$ EXAFS data at both Fe and Zn K-edges for FeZnUf·MoO_4 and FeZnUf·WO_4 are presented in Figure 4. Because the L-edge of tungsten is only ~1 keV higher than the K-edge of zinc, the Zn K-edge data for FeZnUf·WO_4 could only be collected 10.5 $Å^{-1}$ beyond its K-edge without interference from the tungsten L-edge absorption and is thus of more limited resolution.

The first-sphere simulation results for the iron K-edge data are summarized in Table 2. An average first-shell coordination of five or six O or N at 2.02 Å for both FeZnUf·MoO_4 and FeZnUf·WO_4 is found, suggesting that the first-shell coordination environments of the iron sites in FeZnUf·MoO_4 and FeZnUf·WO_4 are very similar. In addition, this can be split into two subshells of scatterers at ca. 1.9 and 2.1 Å, and the two-shell fits afford ϵ^2 values considerably smaller

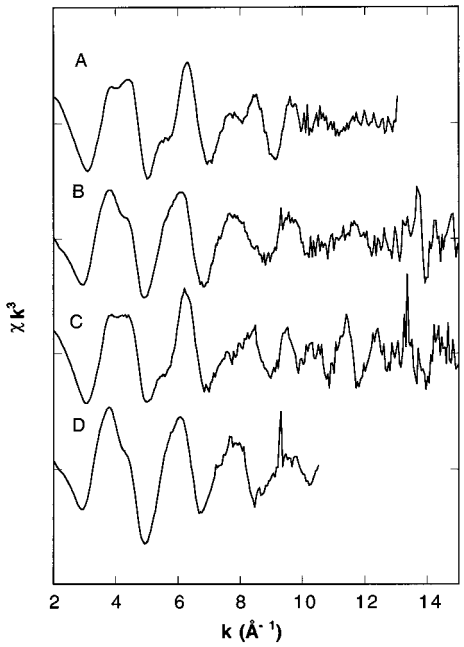

FIGURE 4: Raw EXAFS data ($k^3\chi$) obtained for Fe and Zn K-edges of FeZnUf·MoO_4 (A and B) and FeZnUf·WO_4 (C and D) complexes prepared at pH 4.9.

Table 2: First-Sphere Analysis of the Fourier-Filtered Data[a] (Fe K-Edge)

	Fe−O/N			Fe−O/N			
fit	*n*	*r*	σ^2	*n*	*r*	σ^2	ϵ^2 (×10⁴)
			FeZnUf·MoO_4				
A	6	2.02	0.011				3.3
B	5	2.02	0.009				1.4
C	4	2.05	0.006	2	1.95	0.021	2.2
D	3	2.09	0.004	2	1.95	0.005	1.2
			FeZnUf·WO_4				
A′	6	2.02	0.012				5.5
B′	5	2.02	0.010				5.5
C′	4	2.07	0.004	2	1.91	0.004	2.3
D′	3	2.08	0.002	2	1.93	0.003	0.7

[a] Fourier transform range = 2−13 $Å^{-1}$ for FeZnUf·MoO_4 and 2−15 $Å^{-1}$ for FeZnUf·WO_4. Back-transform range = 1.0−2.0 Å for FeZnUf·MoO_4 and 1.0−2.2 Å for FeZnUf·WO_4.

than those of the one-shell fits. The best fit consists of two shells of two O or N at 1.93−1.95 Å and three O or N at 2.08−2.09 Å (fits D and D′ in Table 2).

Similar to the iron K-edge data, the zinc K-edge data for both FeZnUf·MoO_4 and FeZnUf·WO_4 can be simulated with a single shell of scatterers at 2.07−2.08 Å but with fairly large ϵ^2 values (Table 3). The inclusion of a low-Z scatterer at ca. 2.5 Å makes a notable improvement in ϵ^2 to the fits of both FeZnUf·MoO_4 and FeZnUf·WO_4, as observed in previous EXAFS studies of FeZnUf and FeZnUf·PO_4 (*18*). Furthermore, the higher-resolution data of FeZnUf·MoO_4 make it possible to split the main shell at 2.07 Å into two subshells of four O or N at 2.04 Å and one O or N at 2.22 Å, decreasing the ϵ^2 value by more than 3-fold (fit F in Table 3 and Figure 5) compared to those of the two-shell fits (fits C−E in Table 3).

Outer-Sphere EXAFS Analysis. The Fourier transforms of the filtered $k^3\chi$ EXAFS data are shown in Figure 6. Compared to those of FeZnUf·PO_4 (*18*), the second-sphere features in the Fe K-edge spectra of both FeZnUf·MoO_4 and

Table 3: First-Sphere EXAFS Fits to the Fourier-Filtered Data[a] (Zn K-Edge)

	Zn−O/N			Zn−O/N			Zn−O/C			
fit	*n*	*r*	σ^2	*n*	*r*	σ^2	*n*	*r*	σ^2	ϵ^2 (×10⁴)
				FeZnUf·MoO_4						
A	6	2.07	0.011							10.4
B	5	2.07	0.008							6.1
C	5	2.07	0.008				1	2.50	0.003	2.8
D	4	2.07	0.006				1	2.52	0.004	3.4
E	4	2.04	0.004	1	2.21	0.0005				4.2
F	3	2.04	0.004	1	2.22	0.002	1	2.52	0.003	0.8
				FeZnUf·WO_4						
A′	6	2.08	0.010							8.7
B′	5	2.08	0.007				1	2.52	0.003	0.6

[a] Fourier transform range = 2−15 $Å^{-1}$ for FeZnUf·MoO_4 and 2−10.5 $Å^{-1}$ for FeZnUf·WO_4. Back-transform range = 1−2.3 Å.

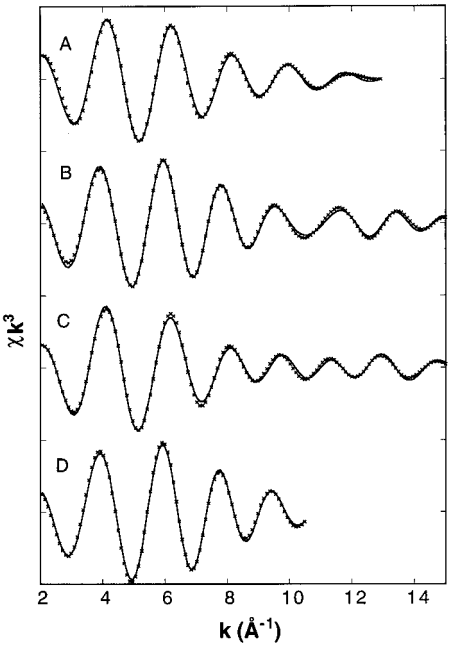

FIGURE 5: Fourier-filtered $k^3\chi$ EXAFS data (×) and first-sphere fits (−) of Fe and Zn K-edges of FeZnUf·MoO_4 (A and B) and FeZnUf·WO_4 (C and D).

FeZnUf·WO_4 are stronger; particularly prominent is a feature around $R' = 3.0$ Å in the tungstate complex. The inclusion of a Zn scatterer at 3.4 Å significantly decreases the ϵ^2 value (fit A in Table 4), as does the introduction of a Mo scatterer at 3.2 Å for the FeZnUf·MoO_4 Fe K-edge fits (fit B in Table 4). This is consistent with previous ESEEM studies on Uf_r·MoO_4, which indicate that molybdate is directly coordinated to the dinuclear center (*36*). The best fit for FeZnUf·MoO_4 consists of a Zn scatterer at 3.43 Å and a Mo scatterer at 3.19 Å (fit E in Table 4). An alternative fit with a Zn shell at ∼3.4 Å and a C shell at ∼3.0 Å was attempted, but the ϵ^2 value of the fit was too high to be reasonable and the Debye−Waller factor for the C shell was negative (fit D in Table 4). Similarly, the best fit for FeZnUf·WO_4 requires a Zn scatterer at 3.41 Å and a W scatterer at 3.21 Å (fit E′ in Table 4). While the alternative fit with a Zn scatterer at 3.4 Å and a C scatterer at 3.0 Å affords a slightly smaller ϵ^2 value, the Debye−Waller factors for both Zn (0.002) and C shells (0.0002) are much too small to be reasonable for such long distances.

Table 4: Outer-Sphere Fits to the Fourier-Filtered $k^3\chi$ Data (Fe K-Edge)

	Fe−Zn			Fe−Mo (or W)			Fe−C				
fit	*n*	*r*	σ^2	*n*	*r*	σ^2	*n*	*r*	σ^2	ϵ^2 ($\times 10^4$)[a]	ϵ^2 ($\times 10^4$)[b]
						FeZnUf·MoO_4					
A	1	3.39	0.005							8.0	
B				1	3.21	0.006				6.7	
C							2	3.07	−0.002	16.5	
D	1	3.40	0.005				2	3.06	−0.001	5.8	
E	1	3.43	0.006	1	3.19	0.006				2.4	6.8
F	1	3.43	0.006	1	3.19	0.006	7	4.28	0.006		2.5
						FeZnUf·WO_4					
A′	1	3.45	0.002							3.2	
B′				1	3.19	0.004				8.0	
C′							2	3.01	0.0001	19.7	
D′	1	3.45	0.002				2	3.01	0.0002	2.0	
E′	1	3.41	0.005	1	3.21	0.004				2.5	5.6
F′	1	3.41	0.005	1	3.21	0.004	6	4.27	0.006		2.9

[a] Back-transform range = 1−3.5 Å for FeZnUf·MoO_4 and FeZnUf·WO_4, and ϵ^2 values for fits D and D′ in Table 1 used as a basis for the fits in this range are 19.5×10^{-4} and 19.6×10^{-4}, respectively. [b] Back-transform range = 1.0−4.2 Å for FeZnUf·MoO_4 and 1.0−4.0 Å for FeZnUf·WO_4.

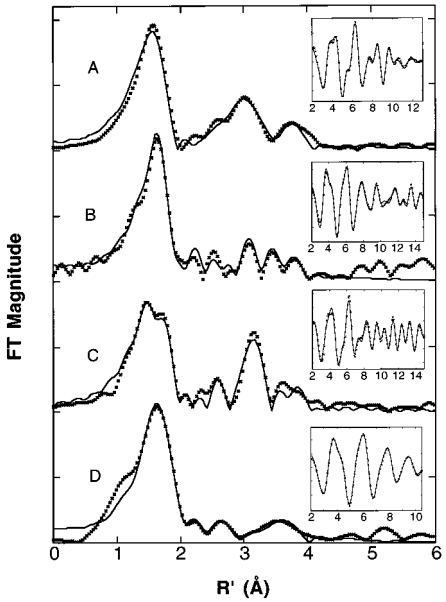

FIGURE 6: Fourier transforms of EXAFS data (×) and outer-sphere fits (—) of Fe and Zn K-edges of FeZnUf·MoO_4 (A and B) and FeZnUf·WO_4 (C and D). Corresponding insets show respective EXAFS data and fits in *k* space.

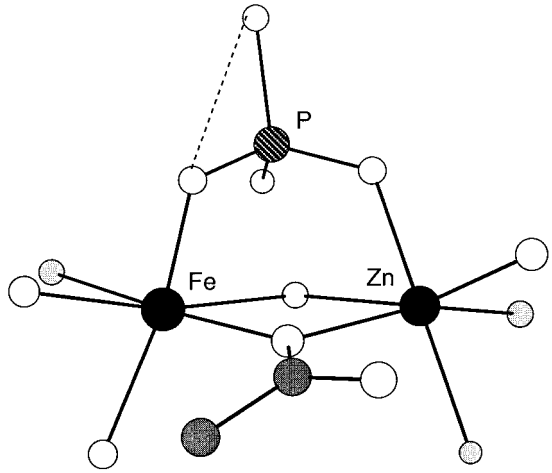

FIGURE 7: Illustration of possible multiple scattering effects from an uncoordinated oxygen atom of the bound phosphate based on the structure of KBPAP·PO_4.

The feature at $R' \sim 3.8$ Å in the Fe K-edges of both molybdate and tungstate complexes can be simulated with a number of low-Z scatterers; these scatterers can be derived from the remote C or N atoms of the histidine ligand and a C_δ atom of the tyrosinate ligand. Another low-Z atom that may contribute to this feature can be identified from an examination of the crystal structures of the KBPAP−anion complexes (*3*). As shown in Figure 7, there is one uncoordinated oxoanion oxygen (O_u) that is ∼ 4.1 Å from the iron. Its contribution to the scattering may be further enhanced by multiple scattering effects due to the near interpolation of a coordinated oxygen atom (O_b) along the Fe−O_u vector forming an Fe−O_b−O_u angle of 170°.

The Zn K-edge R'-space spectrum of FeZnUf·MoO_4 exhibits three well-resolved features between 3 and 4 Å (Figure 6B), including one at 3.5 Å that is not observed in the spectrum of FeZnUf·PO_4. The introduction of an Fe and a Mo scatterer at $R \sim 3.2$ Å does not give rise to a fit with an acceptable Debye−Waller factor for the Fe shell (fit D in Table 5), in contrast to the fitting results for FeZnUf·PO_4 (Fe and Zn K-edges) (*18*) and FeZnUf·MoO_4 (Fe K-edge). However, the combination of a C shell at 3.2 Å and an Fe shell at 3.4 Å affords a good fit with reasonable Debye−Waller factors for both shells (fit E in Table 5). These scatterers account for the $R' = 3.1$ Å feature in Figure 6B. The $R' = 3.8$ Å feature, on the other hand, can be fit with a four-C shell at 4.1 Å. These two carbon shells at 3.2 and 4.1 Å very likely arise from the noncoordinated atoms of the His ligands at the Zn site. This leaves the $R' = 3.5$ Å shell which is fit well with a Mo scatterer at 3.7 Å (fits F and G in Table 5). The Zn K-edge spectrum of FeZnUf·WO_4, though of more limited resolution, can be fit with a similar set of scatterers: one Fe at 3.4 Å, four C at 3.2 Å, one W at 3.6 Å, and four C at 4.1 Å (fit F′ in Table 5).

Taken together, the outer-sphere fits to the Fe and the Zn K-edge data for FeZnUf·MoO_4 and FeZnUf·WO_4 indicate that the two complexes have very similar core structures. The Fe and Zn ions are separated by ∼3.4 Å and bridged unsymmetrically by molybdate or tungstate with Fe−Mo/W distances of 3.2 Å and Zn−Mo/W distances of 3.6−3.7 Å.

Table 5: Outer-Sphere Fits to the Fourier-Filtered $k^3\chi$ Data (Zn K-Edge)

	Zn−Fe			Zn−Mo (or W)			Zn−C			Zn−C				
fit	*n*	*r*	σ^2	*n*	*r*	σ^2	*n*	*r*	σ^2	*n*	*r*	σ^2	ϵ^2 ($\times 10^4$)[a]	ϵ^2 ($\times 10^4$)[b]
							FeZnUf·MoO_4							
A	1	3.38	0.009										4.8	
B				1	3.21	0.010							3.6	
C							4	3.36	0.034				4.6	
D	1	3.13	0.023	1	3.20	0.010							3.4	
E	1	3.37	0.005				4	3.24	0.005				2.9	6.4
F	1	3.37	0.005	1	3.74	0.009	4	3.24	0.006					4.9
G	1	3.37	0.005	1	3.72	0.009	4	3.24	0.006	4	4.12	0.002		3.4
							FeZnUf·WO_4							
A′				1	3.24	0.019							1.3	
B′							4	3.20	0.010				1.1	5.5
C′	1	3.42	0.014				4	3.25	0.007					5.5
D′				1	3.62	0.010	4	3.27	0.016					5.2
E′	1	3.37	−0.001	1	3.66	0.002	4	3.25	−0.007					3.9
F′	1	3.39	0.006	1	3.64	0.009	4	3.24	0.006	4	4.08	0.004		1.0

[a] Back-transform range = 1.1−3.3 Å for FeZnUf·MoO_4 and 1.1−3.0 Å for FeZnUf·WO_4, and ϵ^2 values for fits F and B′ in Table 2 used as a basis for the fits in this range are 5.0×10^{-4} and 2.0×10^{-4}, respectively. [b] Back-transform range = 1.1−4.0 Å for FeZnUf·MoO_4 and FeZnUf·WO_4.

Table 6: EXAFS Analysis of FeZnUf and Its Anionic Complexes at pH 4.9

	first sphere		second sphere
FeZnUf[a]	5 Fe−O/N, 2.02 Å	5 Zn−O/N, 2.02 Å 1 Zn−O/N, 2.46 Å	Fe−Zn, ∼3.3 Å
FeZnUf·PO_4[a]	3 Fe−O/N, 2.12 Å 2 Fe−O/N, 1.94 Å (avg Fe−O/N, 2.01 Å)	3 Zn−O/N, 2.10 Å 2 Zn−O/N, 1.96 Å (avg, 2.02 Å) 1 Zn−O/N, 2.45 Å	Fe−Zn, ∼3.3 Å Fe−P, 3.23 Å Zn−P, 3.19 Å
FeZnUf·MoO_4[b]	3 Fe−O/N, 2.09 Å 2 Fe−O/N, 1.95 Å (avg Fe−O/N, 2.02 Å)	4 Zn−O/N, 2.06 Å 1 Zn−O/N, 2.22 Å (avg, 2.07 Å) 1 Zn−O/N, 2.52 Å	Fe−Zn, ∼3.4 Å Fe−Mo, 3.19 Å Zn−Mo, 3.72 Å
FeZnUf·WO_4[b]	3 Fe−O/N, 2.08 Å 2 Fe−O/N, 1.93 Å (avg Fe−O/N, 2.02 Å)	5 Zn−O/N, 2.08 Å 1 Zn−O/N, 2.52 Å	Fe−Zn, ∼3.4 Å Fe−W, 3.21 Å Zn−W, 3.64 Å

[a] From ref *18*. [b] From this work.

DISCUSSION

The X-ray absorption spectroscopic analysis of FeZnUf·MoO_4 and FeZnUf·WO_4 indicates that molybdate and tungstate interact with the dinuclear center of uteroferrin in a similar fashion. This conclusion is consistent with the steady-state kinetic results showing both molybdate and tungstate to be strong inhibitors of uteroferrin, unlike phosphate which inhibits the enzyme 3 orders of magnitude more weakly (*17*, *37*).

The pre-edge data suggest that both FeZnUf·MoO_4 and FeZnUf·WO_4 have six-coordinate iron sites, in agreement with recent CD and MCD studies (*21*). The average Fe−ligand distances of the iron sites are 2.02 Å for both FeZnUf·MoO_4 and FeZnUf·WO_4, very close to those of FeZnUf and FeZnUf·PO_4 reported previously (Table 6) (*18*). For all three inhibitor complexes, the first sphere can further be resolved into two shells of two O or N scatterers at 1.93−1.95 Å and three O or N scatterers at ca. 2.1 Å. The shorter Fe−ligand bonds very likely correspond to the terminal tyrosinate (1.9 Å) (*38*−*41*) and the bridging hydroxide (1.95 Å) (*42*−*45*), while the longer bonds are associated with the two Asp residues, the His, and the XO_4 oxygen. These results strongly suggest that the iron coordination environment does not change significantly with the binding of molybdate or tungstate.

On the other hand, molybdate and tungstate binding elicits a zinc coordination environment somewhat different from that found in the phosphate complex. When the 2.5 Å scatterer common to all three anion complexes is excluded, the average Zn−ligand distances of FeZnUf·MoO_4 and FeZnUf·WO_4 are 2.07 and 2.08 Å, respectively, about 0.05 Å longer than those found for FeZnUf and FeZnUf·PO_4 (Table 6) (*18*). The higher resolution of the FeZnUf·MoO_4 Zn K-edge data allows the 2.07 Å shell to be split further into two subshells of four scatterers at 2.04 Å and one scatterer at 2.22 Å. Since the NMR spectrum of Uf_r·MoO_4 is not significantly different from that of Uf_r (*46*), the scatterer at 2.22 Å very likely arises from a coordinated molybdate oxygen. So far, there is no available structure of a zinc−molybdate complex for comparison, but the 2.22 Å M−O bond length is longer than those found for a number of diiron(III) molybdate complexes (1.9−2.0 Å) (*47*, *48*). Therefore, the 2.22 Å Zn−O(molybdate) bond suggests that molybdate binds to the Zn site weakly and other binding interactions are more important.

As previously reported for FeZnUf·PO_4 (*18*), a scatterer at 2.5 Å on the Zn site is also required in the fits for both FeZnUf·MoO_4 and FeZnUf·WO_4. Since no such long Zn−ligand bond is found in the crystal structure of KBPAP (*2*, *3*), there are two possible assignments for this scatterer as previously discussed in detail for the phosphate complex.

The 2.5 Å scatterer may be associated with the Asn ligand that is trans to the hydroxo bridge, by analogy to the Asn ligand in the active site of soybean lipoxygenase that is reported to be bound 3 Å from the metal center (*49*). Alternatively, the 2.5 Å scatterer may arise from the N_ϵ-bound His which is not observed in the NMR spectra of Uf_r complexes (*46*) and thus may be weakly bound to the Zn site.

The EXAFS analysis of both the iron and zinc K-edge data demonstrates that the Fe−Zn distances of FeZnUf·MoO_4 and FeZnUf·WO_4 are ∼3.4 Å, slightly longer than the metal−metal distance found for the EXAFS-derived structure of FeZnUf·PO_4 (3.3 Å) (*18*). The elongation of the Fe−Zn distance is consistent with the somewhat larger bite angle expected for a bridging molybdate or tungstate relative to phosphate. Similarly, the Fe−Fe distance of the diiron(III) site of oxidized uteroferrin is modulated by the binding of phosphate and arsenate (*50*). This effect of the bite angle is also illustrated in a series of (μ-oxo)diiron(III) complexes supported by an additional three-atom bridge (*47*), where the Fe−Fe distance increases from 3.25 to 3.4 Å with carboxylate, phosphate, and molybdate acting as the bidentate bridge. The EXAFS-determined Fe−Zn distance is also in agreement with metal−metal distances found in the crystal structures of KBPAP (3.26 Å) (*2*, *3*) and related phosphatases with a (μ-hydroxo)(μ,η^1-aspartato)dimetal core (*4*−*7*).

The EXAFS analyses of the Fe K-edge spectra of both FeZnUf·MoO_4 and FeZnUf·WO_4 require the inclusion of a Mo or W scatterer ∼3.2 Å from the Fe center. This is dramatically demonstrated by the appearance of an intense peak at $R' \sim 3$ Å in the Fourier-transformed spectrum of the WO_4 complex relative to that of the MoO_4 complex (Figure 6), consistent with the stronger scattering expected for the heavier atom. The 3.2 Å distance is shorter than the 3.35−3.65 Å distances observed for diiron(III) complexes bridged by MoO_4 or WO_4 (*47*, *48*, *51*, *52*). Correspondingly, the calculated Fe−O−Mo/W angle of ca. 115° for the FeZnUf−anion complexes, assuming an Fe−OXO_3 (X = Mo or W) bond length of 2.0 Å and an X−O bond length of 1.75 Å, is also more acute than the angles found for synthetic complexes (125−155°) (*47*, *48*, *51*, *52*). It is thus clear that molybdate and tungstate interact strongly with the Fe(III) site of the PAPs.

In contrast, the interaction of molybdate and tungstate with the Zn(II) site of uteroferrin appears to be significantly weaker. Besides the longer Zn−$OMoO_3$ bond required in the first-sphere fit for FeZnUf·MoO_4, the Zn−Mo/W distances of 3.6−3.7 Å are longer than the corresponding Fe−Mo/W distances. These Zn−Mo distances and the calculated Zn−O−Mo angle of 139° however are typical of diiron complexes with molybdate or tungstate bridges (*47*, *48*, *51*, *52*). Thus, molybdate and tungstate appear to bridge the dinuclear center of FeZnUf in an unsymmetric fashion. Unsymmetric anion bridges to bimetallic units in synthetic complexes are not unusual; often, the asymmetry results from the differing donor strengths of the ligands trans to the anion bridge (*47*, *53*). A particularly dramatic example is the diiron(II) complex [Fe_2(μ-OBz)(XDK)($ImH)_2$(OBz)(MeOH)] (*54*), with Fe−O(carboxylato bridge) bond lengths of 2.04 and 2.20 Å and Fe−O−C angles of 102 and 178°, respectively.

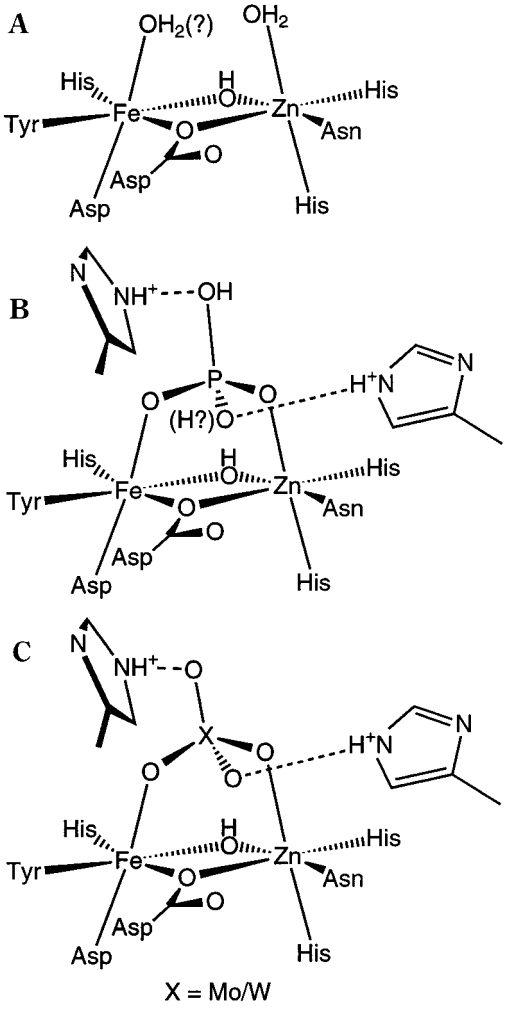

FIGURE 8: Proposed active site structures of (A) FeZnUf, (B) FeZnUf·PO_4, and (C) FeZnUf·MoO_4 and FeZnUf·WO_4 based on EXAFS.

The active site structures of FeZnUf and its three anion complexes deduced from EXAFS are shown in Figure 8 and differ from the crystal structures of KBPAP−anion complexes with respect to the mode of anion binding (*2*, *3*). While the crystal structures of the KBPAP−phosphate and −tungstate complexes both show symmetrically bound anions, the EXAFS results show a symmetric phosphate bridge ($\Delta r_{M-P} = 0.04$ Å) and unsymmetric molybdate and tungstate bridges ($\Delta r_{M-X} > 0.4$ Å). The unsymmetric bridging mode of the molybdate relative to phosphate is also reflected in a comparison of the first-sphere fits for the zinc sites of these anion complexes (Table 6). The average Zn−ligand bond length in FeZnUf·MoO_4 is 0.05 Å longer than that found in FeZnUf·PO_4, a difference that can be explained by the replacement of one of the short 1.96 Å bonds of FeZnUf·PO_4 with the longer 2.22 Å bond found in FeZnUf·MoO_4. We propose that the former arises from the Zn−OPO_3 bond while the latter corresponds to the Zn−$OMoO_3$ bond. Such a difference in metal−anion bond length will affect the electronic properties of the divalent metal center and can explain why the Fe(III)Fe(III)/Fe(II)Fe(III) redox potential of Uf_r·MoO_4 is nearly 400 mV higher than that for Uf_r·PO_4 (*20*), assuming that the conclusions from the FeZnUf fits apply to the diiron enzyme. This in turn justifies why molybdate binding stabilizes Uf_r, while phosphate facilitates

its air oxidation to its inactive Fe(III)Fe(III) form (*17*, *37*).

The significantly higher binding affinities of molybdate and tungstate for the enzyme active site relative to that of phosphate deserve some comment. At pH 4.9, molybdate and tungstate bind to uteroferrin 3 orders of magnitude more strongly than phosphate (*17*, *37*). Since all three anions bridge the dinuclear active site, the binding affinities of these oxoanions must be determined by their interactions not only with the dinuclear center but also with protein residues. The crystal structures of the KBPAP−anion complexes show that all four oxygen atoms of the tetraoxo anion are involved in binding. Besides the two metal ions, the anions also interact with His296 and His202, residues which are conserved in uteroferrin (*3*, *12*). One of these His residues very likely acts as the acid that protonates the departing alkoxide ion during phosphate ester hydrolysis. At pH 4.9 (optimum pH for uteroferrin), these residues are almost certainly protonated and act to neutralize the negative charge of the bound oxoanion by hydrogen bonding to the two uncoordinated oxygen atoms of the anion. That these histidine residues are an important factor in binding is further supported by the observation that anions such as $Fe(CN)_6^{3-}$ and $Cr(CN)_6^{3-}$ can bind to the active site but not to the dinuclear center ($K_d \sim 2$ mM) (*55*, *56*).

Molybdate is a dianion at this pH [p$K_1 = 3.65$, p$K_2 = 3.5$ (*57*)], as is tungstate, so the $HisH^+$−anion interactions would be expected to be strong. These interactions may be more important than the interaction with the divalent site and result in the unsymmetric bridging mode indicated by the EXAFS analysis. On the other hand, phosphate at pH 4.9 is a monoanion (p$K_1 = 2.15$, p$K_2 = 7.10$), and both uncoordinated oxygen atoms in the $FeZnUf{\cdot}PO_4$ complex may be protonated (*58*). There would then be a weaker attraction between the positively charged His residues and the phosphate, which may result in a stronger interaction with the divalent ion, giving rise to the symmetric bridging mode of the phosphate. This diminished attraction to the $HisH^+$ residues would also account for the much lower affinity of phosphate for the active site and ensures its displacement by substrate from the active site during catalytic turnover. Support for this notion comes from a comparison of K_i values for phosphate and molybdate at various pHs (Table 1 and Figure 2), which increase as the pH rises from 4.0 to 7.5. There are two apparent pK values of ∼5.5 and ∼7.0, which may be ascribed to the sequential ionization of the two $HisH^+$ residues that interact with the oxoanions. While the affinities of molybdate and phosphate differ by a factor of 1000 at pH 4 when both His residues are protonated, they only differ by a factor of 30 at pH 7.5 when both His residues are neutral.

In summary, our EXAFS studies further refine the picture of the purple acid phosphatase active site that has been developed with X-ray crystallography. Tetraoxo anions interact with the active site using all four oxygen atoms (Figure 8), and these interactions determine the affinity of the anion for the active site. Two coordinate to the individual metal ions forming a bidentate bridge to the dinuclear center, while the other two hydrogen bond with conserved but unligated His residues in the active site. These His residues probably play important roles in the catalytic mechanism by orienting the substrate and acting as the general acid for hydrolysis (*1*). The most important bioinorganic question that remains to be clarified is the roles the individual metal ions of the dinuclear center play in the hydrolytic mechanism. The numerous and well-characterized spectroscopic properties of uteroferrin and its metal-substituted derivatives provide a basis for tackling this question and establishing a mechanistic paradigm for hydrolysis at a bimetallic enzyme site.

REFERENCES

1. Sträter, N., Lipscomb, W. N., Klabunde, T., and Krebs, B. (1996) *Angew. Chem., Int. Ed. Engl. 35*, 2024−2055.
2. Sträter, N., Klabunde, T., Tucker, P., Witzel, H., and Krebs, B. (1995) *Science 268*, 1489−1492.
3. Klabunde, T., Sträter, N., Fröhlich, R., Witzel, H., and Krebs, B. (1996) *J. Mol. Biol. 259*, 737−748.
4. Egloff, M.-P., Cohen, P. T. W., Reinemer, P., and Barford, D. (1995) *J. Mol. Biol. 254*, 942−959.
5. Goldberg, J., Huang, H.-B., Kwon, Y.-G., Greengard, P., Nairn, A. C., and Kuriyan, J. (1995) *Nature 376*, 745−753.
6. Griffith, J. P., Kim, J. L., Kim, E. E., Sintchak, M. D., Thomson, J. A., Fitzgibbon, M. J., Fleming, M. A., Caron, P. R., Hsiao, K., and Navia, M. A. (1995) *Cell 82*, 507−522.
7. Kissinger, C. K., Parge, H. E., Knighton, D. R., Lewis, C. T., Pelletier, L. A., Tempczyk, A., Kalish, V. J., Tucker, K. D., Showalter, R. E., Moomaw, E. W., Gastinel, L. N., Habuka, N., Chen, X., Maldonado, F., Barker, J. E., Bacquet, R., and Villafranca, J. E. (1995) *Nature 378*, 641−644.
8. Vincent, J. B., and Averill, B. A. (1990) *FEBS Lett. 263*, 265−268.
9. Rusnak, F., Yu, L., and Mertz, P. (1996) *J. Biol. Inorg. Chem. 1*, 388−396.
10. Dent, P., Lavoinne, A., Nakielny, S., Caudwell, F. B., Watt, P., and Cohen, P. (1990) *Nature 348*, 302−307.
11. Liu, J., Farmer, J. D., Jr., Lane, W. S., Friedman, J., Weissman, I., and Schreiber, S. L. (1991) *Cell 66*, 807−815.
12. Klabunde, T., Sträter, N., Krebs, B., and Witzel, H. (1995) *FEBS Lett. 367*, 56−60.
13. Keough, D. T., Beck, J. L., de Jersey, J., and Zerner, B. (1982) *Biochem. Biophys. Res. Commun. 108*, 1643−1648.
14. Davis, J. C., and Averill, B. A. (1982) *Proc. Natl. Acad. Sci. U.S.A. 79*, 4623−4627.
15. Beck, J. L., McArthur, M. J., de Jersey, J., and Zerner, B. (1988) *Inorg. Chim. Acta 153*, 39−44.
16. Suerbaum, H., Körner, M., Witzel, H., Althaus, E., Mosel, B.-D., and Müller-Warmuth, W. (1993) *Eur. J. Biochem. 214*, 313−321.
17. David, S. S., and Que, L., Jr. (1990) *J. Am. Chem. Soc. 112*, 6455−6463.
18. Wang, X., Randall, C. R., True, A. E., and Que, L., Jr. (1996) *Biochemistry 35*, 13946−13954.
19. Antanaitis, B. C., and Aisen, P. (1985) *J. Biol. Chem. 260*, 751−756.
20. Wang, D. L., Holz, R. C., David, S. S., Que, L., Jr., and Stankovich, M. T. (1991) *Biochemistry 30*, 8187−8194.
21. Yang, Y.-S., McCormick, J. M., and Solomon, E. I. (1997) *J. Am. Chem. Soc. 119*, 11832−11842.
22. Basha, S. M., Bazer, F. W., Geisert, R. D., and Roberts, R. M. (1980) *J. Anim. Sci. 50*, 113−123.
23. Pyrz, J. W., Sage, J. T., Debrunner, P. G., and Que, L., Jr. (1986) *J. Biol. Chem. 261*, 11015−11020.
24. Keough, D. T., Dionysius, D. A., deJersey, J., and Zerner, B. (1980) *Biochem. Biophys. Res. Commun. 94*, 600−605.
25. Scott, R. A. (1985) *Methods Enzymol. 11*, 414−459.
26. Teo, B.-K. (1981) *EXAFS Spectroscopy, Techniques and Applications*, pp 13−58, Plenum, New York.
27. Scarrow, R. C., Maroney, M. J., Palmer, S. M., Que, L., Jr., Roe, A. L., Salowe, S. P., and Stubbe, J. (1987) *J. Am. Chem. Soc. 109*, 7857−7864.
28. Teo, B.-K., and Lee, P. A. (1979) *J. Am. Chem. Soc. 101*, 2815−2832.
29. McKale, A. G., Veal, B. W., Paulikas, A. P., Chan, S.-K., and Knapp, G. S. (1988) *J. Am. Chem. Soc. 110*, 3763−3768.

30. Teo, B.-K., Antonio, M. R., and Averill, B. A. (1983) *J. Am. Chem. Soc. 105*, 3751−3762.
31. Bunker, G., Hasnain, S., and Sayers, D. (1991) in *X-ray Absorption Fine Structure* (Hasnain, S. S., Ed.) pp 751−770, Ellis Horwood, New York.
32. Riggs-Gelasco, P. J., Stemmler, T. L., and Penner-Hahn, J. E. (1995) *Coord. Chem. Rev. 144*, 245−286.
33. Stern, E. A. (1993) *Phys. Rev. B. 48*, 9825−9827.
34. Roe, A. L., Schneider, D. J., Mayer, R. J., Pyrz, J. W., Widom, J., and Que, L., Jr. (1984) *J. Am. Chem. Soc. 106*, 1676−1681.
35. Randall, C. R., Shu, L., Chiou, Y.-M., Hagan, K. S., Ito, M., Kitajima, N., Lachicotte, R. J., Zang, Y., and Que, L., Jr. (1995) *Inorg. Chem. 34*, 1036−1039.
36. Doi, K., McCracken, J., Peisach, J., and Aisen, P. (1988) *J. Biol. Chem. 263*, 5757−5763.
37. Pyrz, J. W. (1986) Ph.D. Dissertation, Cornell University, Ithaca, NY.
38. Davis, J. C., Kung, W. S., and Averill, B. A. (1986) *Inorg. Chem. 25*, 394−396.
39. Heistand, R. H., II, Roe, A. L., and Que, L., Jr. (1982) *Inorg. Chem. 21*, 676−681.
40. Lauffer, R. B., Heistand, R. H., II, and Que, L., Jr. (1983) *Inorg. Chem. 22*, 50−55.
41. Pyrz, J. W., Pan, X., and Que, L., Jr. (1991) *Inorg. Chem. 30*, 3462−3464.
42. Armstrong, W. H., and Lippard, S. J. (1984) *J. Am. Chem. Soc. 106*, 4632−4633.
43. Bossek, U., Hummel, H., Weyhermüller, T., Bill, E., and Wieghardt, K. (1995) *Angew. Chem., Int. Ed. Engl. 34*, 2642−2645.
44. Thich, J. A., Oh, C. C., Powers, D., Vasilou, B., Mastropaolo, D., Potenza, J. A., and Schugar, H. J. (1976) *J. Am. Chem. Soc. 98*, 1425−1433.
45. Turowski, P. N., Armstrong, W. H., Liu, S., Brown, S. N., and Lippard, S. J. (1994) *Inorg. Chem. 33*, 636−645.
46. Scarrow, R. C., Pyrz, J. W., and Que, L., Jr. (1990) *J. Am. Chem. Soc. 112*, 657−665.
47. Holz, R. C., Elgren, T. E., Pearce, L. L., Zhang, J. H., O'Connor, C. J., and Que, L., Jr. (1993) *Inorg. Chem. 32*, 5844−5850.
48. Lettko, K., Liu, S., and Zubieta, J. (1991) *Acta Crystallogr. C47*, 1723.
49. Minor, W., Steczko, J., Stec, R., Otwinowski, Z., Bolin, J. T., Walter, R., and Axelrod, B. (1996) *Biochemistry 35*, 10687−10701.
50. True, A. E., Scarrow, R. C., Randall, C. R., Holz, R. C., and Que, L., Jr. (1993) *J. Am. Chem. Soc. 115*, 4246−4255.
51. Chaudhuri, P., Winter, M., Wieghardt, K., Gehring, S., Haase, W., Nuber, B., and Weiss, J. (1988) *Inorg. Chem. 27*, 1564−1569.
52. Chaudhuri, P., Weighardt, K., Nuber, B., and Weiss, J. (1987) *J. Chem. Soc., Chem. Commun.*, 1198−1199.
53. Norman, R. E., Yan, S., Que, L., Jr., Backes, G., Ling, J., Sanders-Loehr, J., Zhang, J., and O'Connor, C. J. (1990) *J. Am. Chem. Soc. 112*, 1554−1562.
54. Herold, S., Pence, L. E., and Lippard, S. J. (1995) *J. Am. Chem. Soc. 117*, 6134−6135.
55. Aquino, M. A. S., and Sykes, A. G. (1994) *J. Chem. Soc., Dalton Trans.*, 683−687.
56. Lim, J.-S., Aquino, M. A. S., and Sykes, A. G. (1996) *Inorg. Chem. 35*, 614−618.
57. Aveston, J., Anacker, E. W., and Johnson, J. S. (1964) *Inorg. Chem. 3*, 735−746.
58. Aquino, M. A. S., Lim, J.-S., and Sykes, A. G. (1994) *J. Chem. Soc., Dalton Trans.*, 429−436.

BI980150A